JGR Space Physics

RESEARCH ARTICLE
10.1029/2025JA034221

The Impact of Geomagnetic Activity on the Height-Dependent Ionospheric Delay in Relation to Solar Activity

Rajesh Vaishnav[1], Christoph Jacobi[1], Erik Schmölter[2], and Hanna Dühnen[2]

[1]Leipzig Institute for Meteorology, Leipzig University, Leipzig, Germany, [2]German Aerospace Center, Neustrelitz, Germany

Key Points:

- The ionospheric delay observed in electron density increases with altitude up to 300 km
- Geomagnetic activity significantly impacts the altitude-dependent ionospheric delay
- The changes in the ionospheric delay are associated with changes in the O/N_2 ratio

Correspondence to:

R. Vaishnav,
rajesh_ishwardas.vaishnav@uni-leipzig.de

Citation:

Vaishnav, R., Jacobi, C., Schmölter, E., & Dühnen, H. (2025). The impact of geomagnetic activity on the height-dependent ionospheric delay in relation to solar activity. *Journal of Geophysical Research: Space Physics*, *130*, e2025JA034221. https://doi.org/10.1029/2025JA034221

Received 22 MAY 2025
Accepted 11 OCT 2025

Abstract Previous research has indicated that geomagnetic activity plays an important role in influencing the ionospheric delayed response to solar activity variations at the solar rotation time scale depending on solar activity conditions. In this study, we employed the Thermosphere-Ionosphere-Electrodynamic General Circulation Model to investigate the vertically resolved impact of geomagnetic activity on the ionospheric delay over the solar rotation period from 29 April to 25 May 2015. This time period was chosen due to its representative moderate solar and geomagnetic activity conditions. Our analysis revealed that the ionospheric delay increases with altitude due to geomagnetic activity and is more pronounced in the Southern Hemisphere than in the Northern Hemisphere. To further understand the underlying mechanisms responsible for the observed changes in ionospheric delay, we examined neutral species (O and N_2), their ratio (O/N_2), and neutral temperature. The results show that thermosphere-ionosphere composition varies both vertically and horizontally in response to geomagnetic activity, and that these composition changes contribute to vertical variations in ionospheric delay.

1. Introduction

The complex thermosphere-ionosphere (TI) system is strongly varying both temporally and spatially due to external forcing such as solar activity, geomagnetic activity, and influences from the lower atmosphere (e.g., Fang et al., 2013; Forbes et al., 2000; Rishbeth & Mendillo, 2001, and references therein). The TI shows variations across multiple timescales, including a notable approximately 27-day periodicity linked to solar rotation (e.g., Afraimovich et al., 2008; Chen et al., 2012; Kutiev et al., 2013; Liu et al., 2006, and references therein). Several authors have investigated the relationship between solar activity indices and ionospheric-thermospheric parameters specifically at the 27-day solar rotation period (e.g., Afraimovich et al., 2008; Anderson & Hawkins, 2016; Chen et al., 2012; Jakowski et al., 1991; Kutiev et al., 2013; Liu et al., 2006, and references therein).

Apart from solar activity, geomagnetic activity serves as an important factor influencing the neutral components of the TI, particularly O and N_2. These neutral constituents play a crucial role in various processes within the TI system. During geomagnetic storms, Joule heating and particle precipitation at high latitudes significantly alter upper atmospheric composition by upwelling N_2-rich and O-depleted air from lower altitudes. Neutral winds then transport these composition perturbations to mid-latitudes, causing O/N_2 ratio depletion. This storm-induced redistribution of neutral species directly impacts ionospheric F_2 region electron density, where photochemical processes, such as the photoionization of O and the recombination of O^+ by N_2 compete (e.g., D. Strickland et al., 2004; Thayer & Semeter, 2004; Sutton et al., 2009, and references therein). Therefore, the ratio of O to N_2 is closely connected to the electron density (Rishbeth, 1998). Additionally, transport processes, including neutral winds and diffusion, also contribute to shaping electron densities, as demonstrated in preceding studies (e.g., Burns et al., 2004; Cai et al., 2021; Fuller-Rowell et al., 1994; Qian et al., 2020; Rishbeth et al., 2000).

The 27-day periodicity in the ionospheric parameters as the peak electron density of the F_2 layer (NmF2), total electron content (TEC), temperature, and neutral densities is related to the solar rotation period, whose solar flux amplitude significantly varies based on the solar activity conditions (Kutiev et al., 2013). However the reaction of the ionospheric electron density is not immediate and the electron density peak is observed with a certain delay as compared to the peak of the solar flux during the solar rotation period. This peak time difference is known as the ionospheric delayed response, and it amounts to about 18 hr to 2 days. This feature has been investigation by several authors using different ionospheric observations (e.g., Afraimovich et al., 2008; Jacobi et al., 2016; Ren et al., 2018; Schmölter et al., 2018, 2021) and numerical model simulations (e.g., Dühnen et al., 2024; Jakowski

et al., 1991; Ren et al., 2018, 2019; Schmölter et al., 2020a, 2022, 2024; Vaishnav et al., 2018; Vaishnav, Jacobi, Schmölter, & Dühnen, 2024; Vaishnav, Jacobi, et al., 2021; Vaishnav, Schmölter, et al., 2021).

Previous research has shown that the ionospheric delay is influenced by several factors, including solar activity (e.g., Schmölter et al., 2024; Vaishnav, Schmölter, et al., 2021), lower atmospheric forcing (e.g., Vaishnav, Jacobi, Schmölter, & Dühnen, 2024), and geomagnetic activity (e.g., Ren et al., 2018; Schmölter et al., 2020a, 2020b; Vaishnav et al., 2022). The delayed ionospheric response exhibits seasonal variations influenced by TI processes that are linked to geomagnetic activity (Schmölter et al., 2020b). Previous studies have also reported on the altitudinal dependence of the delayed ionospheric response (Schmölter et al., 2022; Vaishnav et al., 2022). However, a model investigation addressing vertical variations in ionospheric delay due to geomagnetic activity is lacking. This study utilizes the Thermosphere-Ionosphere-Electrodynamics General Circulation Model (TIE-GCM) (e.g., Richmond et al., 1992) to investigates the vertical variations in ionospheric response to solar variability during a moderate storm. We focus on NmF2, TEC, the O/N_2 ratio, the F10.7 index, and geomagnetic indices.

The paper is arranged as follows. Section 2 introduces the data sources and the TIE-GCM. Section 3 presents results on the influence of geomagnetic activity on ionospheric delay. Section 4 discusses our findings and concludes the paper.

2. Observations and Model

The ionospheric state is represented by TEC, which is taken from IGS TEC maps that are derived from a global GNSS network and ionosondes (Hernández-Pajares et al., 2009). The IGS TEC values are available at a spatial resolution of 2.5°/5° and a temporal resolution of 1 hr, provided by the CDDIS data archive service (NASA, 2025a). Daily F10.7 index values are obtained from the LISIRD database (LASP, 2025), while geomagnetic indices (Kp, AE, and Dst) and the By and Bz components of the interplanetary magnetic field (IMF) are sourced from the OmniWeb database (NASA, 2025b).

We used TIE-GCM (version 2.0) simulations to investigate how geomagnetic activity influences the ionospheric delay mechanism. The TIE-GCM is a global, three-dimensional, time-dependent model that simulates thermosphere-ionosphere electrodynamics by solving key equations for composition, dynamics, and energy in the thermosphere (Qian et al., 2014; Richmond & Maute, 2014). The TIEGCM employs a log-pressure vertical coordinate defined as

$$z = \ln(p_0/p), \tag{1}$$

where $p_0 = 5 \times 10^{-5}$ Pa is the reference pressure at the lower boundary (~97 km altitude). The model's 29 pressure levels span $z = -7$ to $+7$, covering altitudes from approximately 97–600 km (depending on solar activity), with a vertical resolution of 0.5 scale heights. The horizontal resolution is 5° × 5° in latitude and longitude.

At the lower boundary, the geopotential height $Z(z_{\text{bot}})$ is specified as a superposition of tidal components:

$$Z(z_{\text{bot}}) = Z_{\text{SD}} + Z_D + Z_A + Z_{nSD} + Z_{nD}, \tag{2}$$

where Z_{SD}, Z_D, Z_A, Z_{nSD}, and Z_{nD} represent contributions from the migrating semidiurnal, migrating diurnal, annual, and non-migrating semidiurnal and diurnal tides, respectively. The background state at this boundary is fixed, with a geopotential height of 96.37 km, a neutral temperature of 181.0 K, and zero neutral winds, independent of seasonal variations.

Above the lower boundary, the geopotential height at each level is computed using the hydrostatic equation:

$$Z(z + \Delta z) = Z(z) + \frac{\Delta z \cdot R^*}{g} \cdot \frac{T_n}{\bar{m}}\left(z + \frac{1}{2}\Delta z\right), \tag{3}$$

where R^* is the gas constant, T_n is the neutral temperature, $\bar{m}$ is the mean molecular mass, and g is the altitude-dependent gravitational acceleration. The geometric height is obtained by correcting the geopotential height Z. In

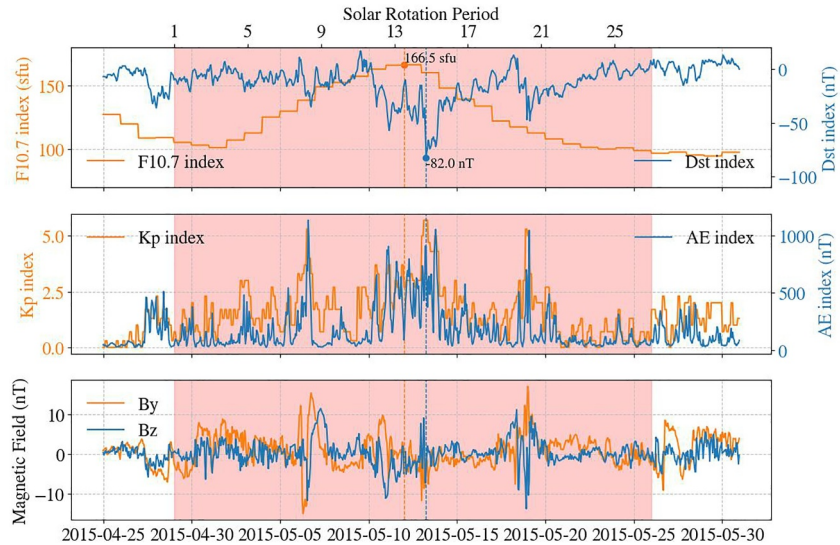

Figure 1. The top panel displays the time series of the F10.7 index (orange line) and the hourly Dst index (blue line) covering the period from 25 April to 30 May 2015. The study period, indicated by the shaded red region, corresponds to the solar rotation from 29 April to 25 May 2015. The second panel features the 3-hr Kp index (orange line) and the AE index (black line). In the third panel, the y (By, orange line) and z (Bz, blue line) components of the interplanetary magnetic field are presented. The orange and blue dashed lines mark the days of the maximum F10.7 index and the minimum Dst index, respectively.

this study, we use linear interpolation in geometric height to convert model outputs from pressure coordinates to the fixed altitude.

For solar input, it utilizes a reference solar spectrum (Richards et al., 1994) driven by variations in the F10.7 solar index. At high-latitudes, it includes ion convection patterns (Heelis et al., 1982) and auroral precipitation (Roble & Ridley, 1987). The aurora depends on hemispheric power (hp), which the TIE-GCM estimates using a 3-hr Kp index. This study focuses on geomagnetic activity from observations and an experiment with Kp $\leq$ 5, using the model's hp values calculated by

$$hp = 16.82 \cdot e^{0.32 \cdot kp} - 4.86 \quad (4)$$

This study aims to investigate the role of geomagnetic activity in altitude-dependent ionospheric delay using the TIE-GCM model simulations.

3. Results

3.1. Geophysical Conditions

We select the study period from 29 April to 25 May 2015, to investigate the impact of geomagnetic activity on the delayed ionospheric response.

Figure 1 illustrates the variations in solar and geomagnetic activity throughout the study period. This time frame is specifically selected based on the season and the levels of solar and geomagnetic activity observed near the peak of the solar rotation. Maximum solar activity occurs on day 14 of the solar rotation period, with the F10.7 index reaching approximately 167 sfu, while the minimum recorded F10.7 index is about 100 sfu. The top panel of Figure 1 shows the absolute values of the hourly Dst index on the right *y*-axis, with the minimum Dst recorded at −82 nT on day 15. The second panel presents the 3-hr Kp index (orange line) and the AE index (blue line). On day 15, the Kp index reaches approximately 6, and a maximum AE of 1,052 nT is observed after a delay of about 10 hr.

In contrast, on day 14, the Kp index remains below 3, while the AE index reaches approximately 700 nT. The third panel displays the IMF components, By and Bz. These components vary significantly between day 14 and day 15,

indicating the onset of the geomagnetic storm and the associated changes in all geomagnetic parameters observed on day 15. The IMF By component reaches negative values of about −12 nT on day 15, while the Bz component remains negative on day 14 and shifts to positive on day 15.

This study focuses on changes in the TI region, specifically in relation to variations in solar and geomagnetic activity. During this period, a moderate storm occurs the day after peak solar activity, providing an excellent opportunity to precisely investigate its direct contribution to ionospheric delay using a numerical model.

Parameters such as TEC, NmF2, and neutral composition in the TI region are significantly influenced by solar and geomagnetic activity, resulting in spatial, temporal, and seasonal variability (Cai et al., 2021; Ren et al., 2018; Schmölter et al., 2020b; Vaishnav, Schmölter, et al., 2021). In this study, we examine the vertical variations in ionospheric delay caused by geomagnetic activity.

3.2. Mechanistic Model Studies

We use the TIE-GCM simulations to illustrate the effect of geomagnetic activity on the TI system. The following simulations are conducted to demonstrate this impact.

1. All Variability Run: The model runs with the default settings (as described in the data section), using the observed F10.7 and the observed Kp index.
2. Solar Variability Run: The model runs with the default settings and observed F10.7, but with Kp fixed at 0.

The TIE-GCM model simulated changes in TI parameters, including NmF2, neutral densities, neutral temperature, neutral wind, and the O/N_2 ratio during the study period.

Figure 2 illustrates the variability of the model-simulated neutral wind at 0° longitude as a function of latitude and altitude at 12 UT. The top panels display the zonal wind for both the Solar and the All Variability Runs. For the Solar Variability Run, the zonal winds are westward in the low-latitude regions and eastward in the moderately high-latitude region of the Northern Hemisphere (NH), as well as in the mid- and high-latitude regions of the Southern Hemisphere (SH) (Figure 2a). Maximum zonal wind occurs at approximately 60°S below 200 km. In contrast, during the All Variability Run, the zonal wind varies strongly in the high-latitude regions. This variation is attributed to geomagnetic moderate storms, which enhance the neutral wind. The strongest zonal wind is observed in the high-latitude areas of the NH (Figure 2b). The zonal winds remain westward in both the low- and mid-latitude regions.

The middle panels of Figure 2 display the meridional wind from both the Solar and All Variability Runs. For the Solar Variability Run, the meridional wind is particularly strong in high-latitude regions. The meridional wind exhibits a poleward direction at mid- and high-latitudes of both hemispheres (Figure 2c). Similar to the Solar Variability Run, the meridional wind in the All Variability Run is also directed poleward. The strong meridional wind observed at high-latitudes reveals significant differences in both the zonal and meridional winds between the two runs. The altitudinal variations of the neutral wind during quiet and storm conditions have been previously discussed by Wang et al. (2008). They suggested that the vertical variations of wind at high-latitudes are a result of altitude-dependent momentum forcing, which is driven by magnetospheric inputs. These inputs enhance pressure gradients, ion drag, and wind shear.

The bottom panels of Figure 2 illustrate the vertical winds (Wn), with positive values indicating upward movement. In most regions of the middle latitudes during the Solar Variability Run, Wn is positive (Figure 2e). Conversely, at high latitudes in the Southern Hemisphere, Wn is predominantly negative (downward). A similar pattern is observed during the All Variability Run as well (Figure 2f). When comparing the All Variability Run to the Solar Variability Run, significant differences appear in the NH high-latitude region. In these region, Wn demonstrates strong positive values at nearly all heights above 150 km, revealing storm-driven thermospheric upwelling.

Li et al. (2019) demonstrated that geomagnetic storms induce altitude-dependent wind responses. During the onset of a storm, horizontal winds in the upper thermosphere experience larger and faster changes compared to winds in the mesosphere and lower thermosphere (MLT). This leads to downward vertical wind perturbations. These effects propagate downward, resulting in reductions in vertical wind throughout the MLT region. This coupled behavior indicates that storm energy penetrates through vertical momentum transfer.

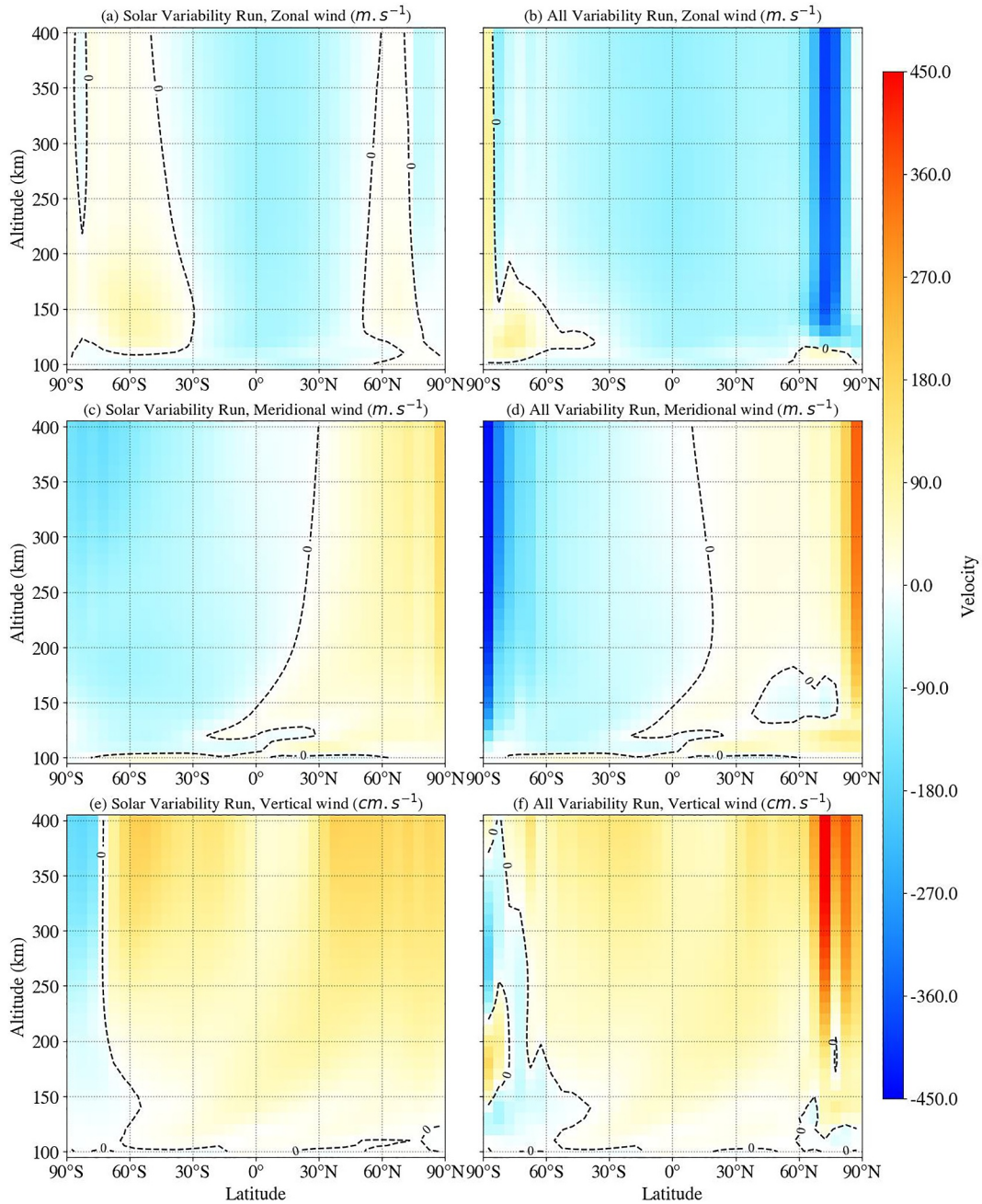

Figure 2. Neutral wind variations for the Solar Variability Run (a, c, e) and All Variability Run (b, d, f) at 12 UT on day 15 as a function of altitude (km) and latitude. Top panels (a, b) show zonal winds, middle panels (c, d) show meridional winds, while bottom panels (e, f) show vertical winds. Please note that the units of neutral wind velocity differ and are indicated in the figure titles. The dashed black lines represent the zero line.

Figure 3 shows the variability of model simulated electron density and O/N_2 ratio at 0° latitude/longitude as a function of day and altitude. The left panel displays the percentage change from the altitude-dependent mean in profiles for the All Variability Run which is calculated as:

$$\text{Percentage change}(z,d) = \frac{N_e(z,d) - \overline{N_e}(z)}{\overline{N_e}(z)} \times 100$$

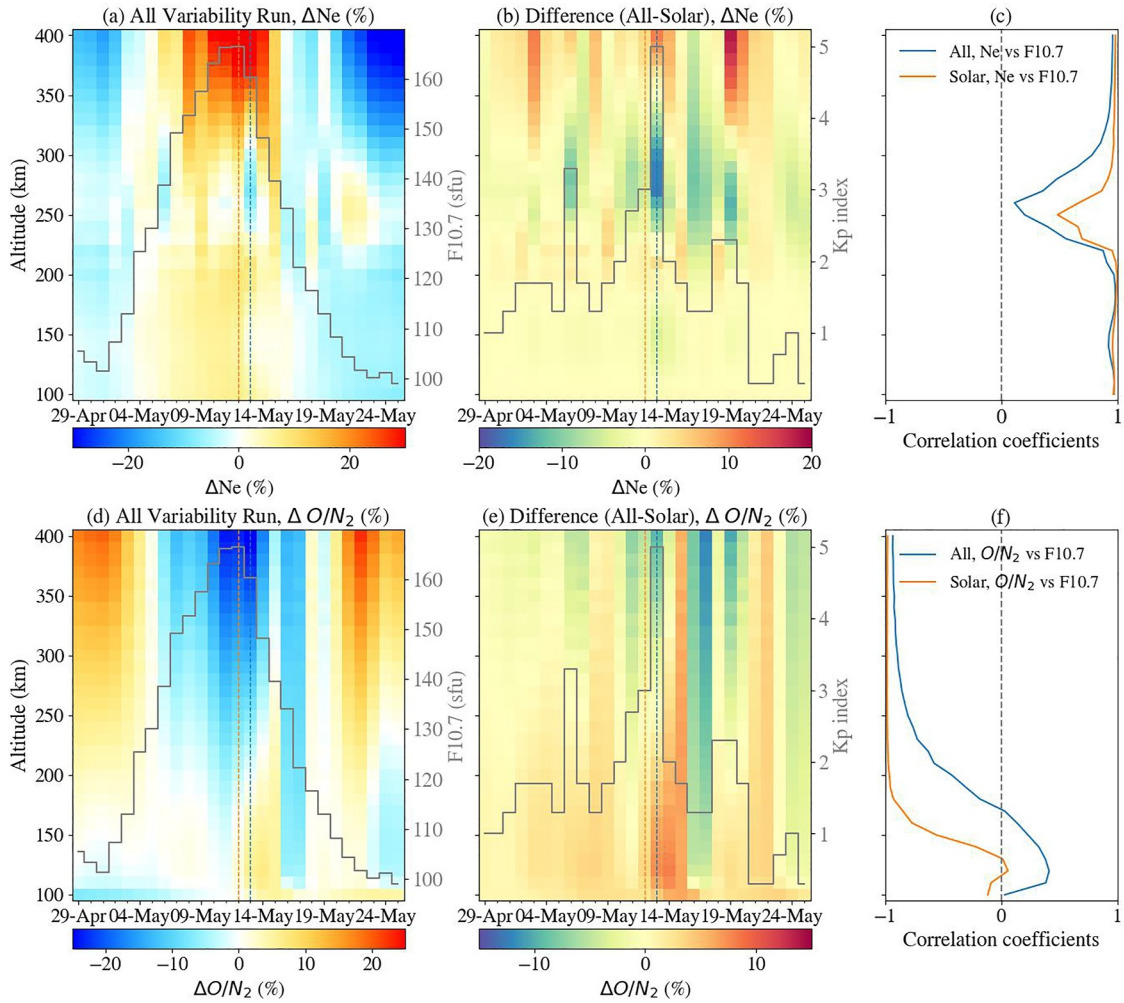

Figure 3. The top panel shows the modeled variations in daily electron density Ne, while the lower panel displays the variations in daily O/N_2, as a function of day and altitude at 0° latitude/longitude for (a, d) the percentage change for All Variability Run and (b, e) the percentage difference ((All Variability—Solar Variability)/Solar Variability). The correlation coefficients of Ne and O/N_2 with the F10.7 index are shown as altitude profiles in (c) and (f), respectively. Blue curves represent All Variability Run, while orange curves represent Solar Variability Run. The right *y*-axis in (a, d), (b, e) represents the F10.7 and Kp index, respectively, in the left and middle panels. The orange and blue dashed lines represent day 14 and day 15, respectively.

Where $N_e(z,d)$ is the electron density at altitude z and day d, and $\overline{N_e}(z)$ is the altitude-dependent mean electron density. The right panel shows the percentage difference between the Solar Variability Run and the All Variability Run ((All Variability - Solar Variability)/Solar Variability). Additionally, the F10.7 (Kp) index is included on the second *y*-axis in the left (middle) panel.

Figure 3a illustrates the evolution of daily electron density in the All Variability Run. Electron density varies with solar activity conditions, increasing with height in the lower F region and reaches maximum values above 300 km. Under moderate solar activity conditions, electron density is also influenced by geomagnetic activity. The maximum increase in electron density, about 25%–35%, occurs above 300 km. In contrast, at altitudes below 220 km, electron density varies by approximately 5%–10% from May 6 to May 18 due to increased solar activity. Figure 3b shows the percentage difference between the All Variability Run and the Solar Variability Run. The maximum difference observed above 300 km ranges between 5% and 10% during the rising solar activity throughout the solar rotation period. Meanwhile, decreases in electron density are noted between 200 and 300 km, with significant day-to-day variations observed after day 15. The largest decrease, approximately 15%, is observed between 250 and 300 km on Day 15 during increased geomagnetic activity.

To investigate the relationship between electron density and solar activity, we calculate the cross-correlation of both the All Variability Run and Solar Variability Run simulated electron densities with the F10.7 index, as shown in Figure 3c. The correlation profiles reveal maximum correlation coefficients of approximately 0.9 below 200 km and again at 320 km. However, the correlation observed between 220 and 320 km is lower, with minimum around 0.2 for the All Variability Run and 0.4 for the Solar Variability Run. The lower panel of Figure 3 shows the variability of the O/N_2 ratio. Figure 3d shows the altitudinal variations on O/N_2 ratio for All Variability Run. Here the O/N_2 ratio is calculated by the mass mixing ratios (mmr) of O and N_2 (N_2 mmr = 1—O mmr—O_2 mmr). The O/N_2 ratio decreases by about 10%–25% above 200 km and decreases with altitude from 6 May to 18 May primarily due to increased solar activity. Below 200 km, a slight increase of about 2%–7% is observed from 13 May to 15 May which can be attributed to increased geomagnetic activity.

The percentage difference between the All and Solar Variability Run is shown in Figure 3e. The O/N_2 ratio slightly increases below 200 km by about 2%–5% while it decreases above 200 km by about 5%–10%. However, there are differences in the day-to-day variability. The cross correlation between the O/N_2 ratio and solar activity is shown in Figure 3f. A negative correlation is observed above 180 km for both All and Solar Variability Run with correlation coefficients of about 0.2–0.9. Below 180 km a slightly positive correlation, which varies from 0.2 to 0.4, exists for the All Variability Run, while correlation coefficients of about 0.1 to −0.8 are observed for the Solar Variability Run.

To understand the variations in the latitudinal behavior of TI parameters, we further investigate the NmF2 and the O/N_2 ratio as function of latitude and day, as shown in Figure 4. The upper panel illustrates the NmF2. NmF2 shows maximum values observed in low-latitude regions and decreases as we move toward higher latitudes in the All Variability Run (Figure 4a). There are significant variation with solar activity, with maximum NmF2 at higher solar activity, but modified by Kp. The difference plot indicates that during peak geomagnetic activity, NmF2 increases by about 50% in the SH, while in the NH, it decreases by approximately 15%–20% (Figure 4b). The lower panel of Figure 4c illustrates the variations in the model-simulated O/N_2 ratio, which is calculated at the height of the maximum F2 layer (HmF2). In the All Variability Run, the maximum O/N_2 ratio is observed in low-latitude regions. Additionally, the SH high-latitude region exhibits a higher O/N_2 ratio compared to the NH. However, these variations are highly dependent on seasonal changes (Qian et al., 2022). Figure 4d displays the percentage difference in the O/N_2 ratio by the two runs. There is approximately a 45% increase in the O/N_2 ratio during periods of maximum geomagnetic activity, followed by moderate activity periods. Under moderate solar activity, we observe a significant influence of geomagnetic activity on both NmF2 and the O/N_2 ratio. Changes in O/N_2 affect the production and loss rates of O^+, the dominant ion in the F region, leading to variations in Ne (Yamazaki & Richmond, 2013).

The electron density strongly depends on the composition of atomic oxygen and molecular nitrogen as well as solar EUV radiation (Rishbeth, 1998). To further explore the relationship between the O/N_2 and Ne at varying altitudes, we calculate the correlation coefficients at 0°E. The aim of calculating the correlation is to observe the relationship between changes in Ne and O/N_2 due to geomagnetic activity.

Figure 5 illustrates the correlation coefficients for both the All Variability Run and the Solar Variability Run as a function of latitude and altitude. In Figure 5a, a positive correlation ranging from approximately 0.1 to 0.6 is observed between altitudes of 200 and 250 km. A slightly positive correlation above 250 km is also visible, but it only occurs in the NH. Additionally, a positive correlation is evident in the low-latitude region from 100 to 320 km. When comparing the All Variability Run to the Solar Variability Run, a slight decrease in correlation is observed in the mid- and high-latitude regions (Figure 5b). In the Solar Variability Run, a positive correlation is noted in the NH's low-latitude region between 250 and 350 km, as well as in the high-latitude region between 150 and 250 km. Over a large range of latitudes/altitudes, however, the correlation is negative, in contrast to the All Variability Run. Furthermore, a strong correlation was observed near 100 km in high-latitude regions and between 170 and 250 km in the SH's high-latitudes. The differences in correlation between these two runs demonstrate the impact of geomagnetic activity on the relationship between O/N_2 and Ne, that is, an increase in correlation owing to geomagnetic variability. Field et al. (1998) examined the relationship between NmF2 and O/N_2 ratio during geomagnetic storms. They found that mid-latitude F-layer storm behavior is mainly driven by composition changes due to thermospheric circulation from high-latitude energy inputs. As a result, NmF2 closely follows the O/N_2 ratio during storms, leading to increased correlation.

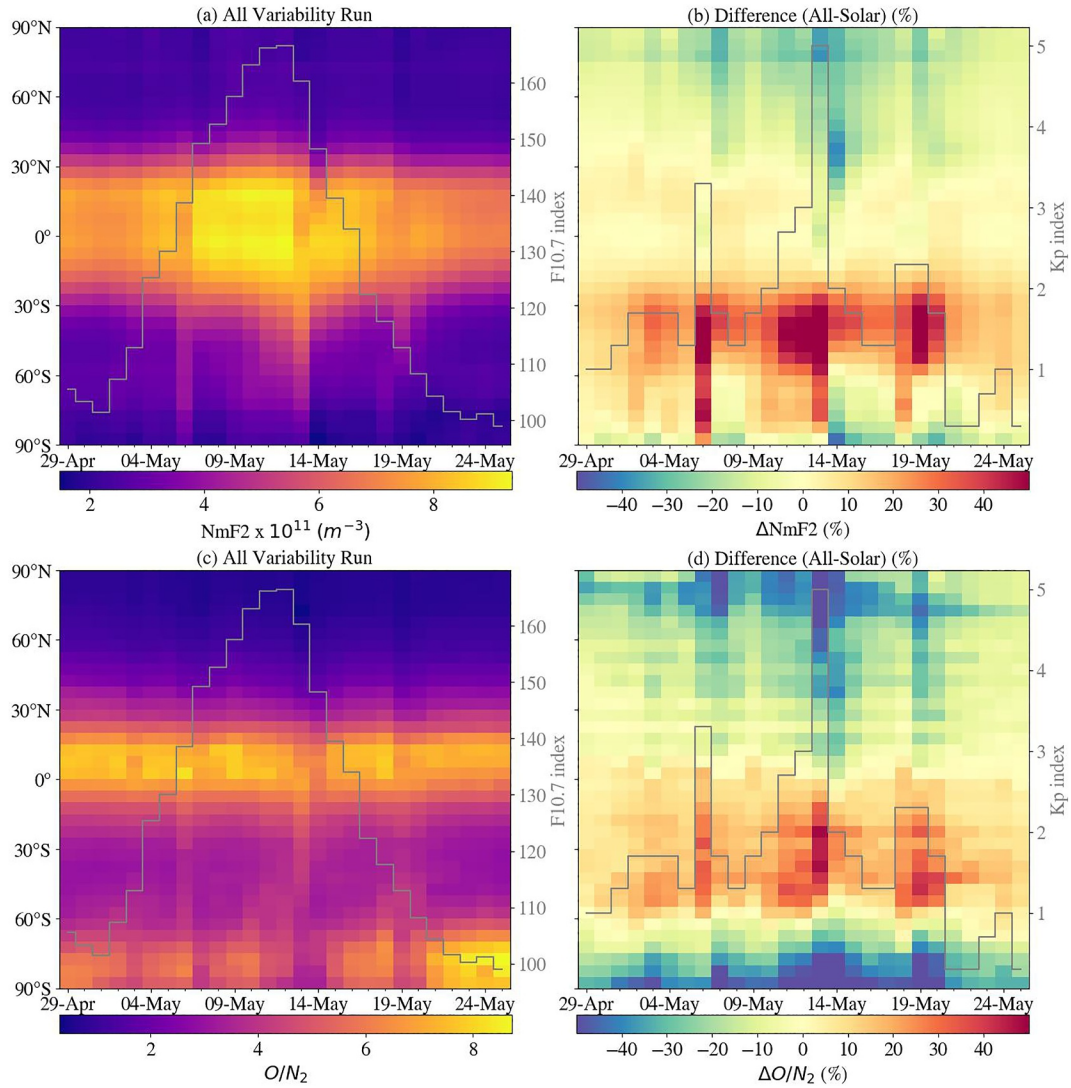

Figure 4. The top panels show the modeled daily NmF2, while the lower panels display the daily O/N_2, as a function of day and latitude for (a, c) the All Variability Run and (b, d) the percentage difference ((All Variability - Solar Variability)/Solar Variability) at 0° longitude. The right *y*-axis in each panel represents the F10.7 and Kp index, respectively, in the left and right panels.

3.3. Delayed Ionospheric Response

Several authors have explored the relationship between variations of solar and TI parameters, reporting a delay of approximately 18 hr to 2 days (e.g., Afraimovich et al., 2008; Jacobi et al., 2016; Jakowski et al., 1991; Ren et al., 2018; Schmölter et al., 2018, 2020a, 2020b, 2021; Vaishnav et al., 2018, 2019; Vaishnav, Jacobi, Berdermann, et al., 2024; Vaishnav, Schmölter, et al., 2021), and an influence of geomagnetic activity (e.g., Ren et al., 2018; Schmölter et al., 2020a, 2020b; Vaishnav et al., 2022).

Here, we calculate the ionospheric delay between the IGS TEC and the modeled NmF2, considering solar activity from 29 April to 25 May 2015. The ionospheric delay is determined using the F10.7 index, as referenced in Vaishnav, Jacobi, Schmölter, and Dühnen (2024). The spatial distribution of the delay is illustrated in Figure 6. The upper panel shows the ionospheric delay between IGS TEC and the F10.7 index. The ionospheric delay is approximately 18 hr, with a higher delay observed in the NH's high-latitude regions, ranging from 30 to 40 hr. In contrast, the SH's high-latitude region exhibits a lower delay of about 5–15 hr. In the mid-latitude regions, the average delay is around 15–25 hr. A similar pattern is evident in the model-simulated TEC for the All Variability Run, however, some differences exist in the high-latitude regions (see Figure 6b). The average delay in the model-

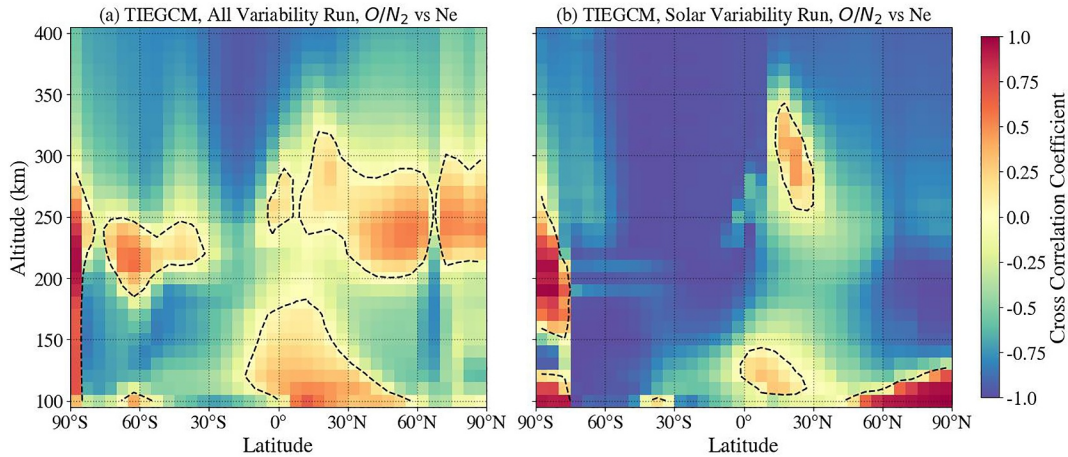

Figure 5. The cross correlation coefficients between the diurnal mean Ne and the O/N_2 ratio simulated by the TIE-GCM for All Variability Run (a) and Solar Variability Run (b) at the 0°E geographic longitude are presented as a function of latitude and altitude. The dashed black line indicates zero correlation coefficients.

simulated data is approximately 17 hr. As geomagnetic activity also influences this period, we calculate the delay using modeled NmF2 for both the All Variability Run and the Solar Variability Run (Figure not shown). The difference between these two runs is illustrated in Figure 6c. The results suggest that due to geomagnetic activity, there is a decrease in delay of about 1–5 hr, except in the NH high-latitude region, where the delay increases by about 3–7 hr.

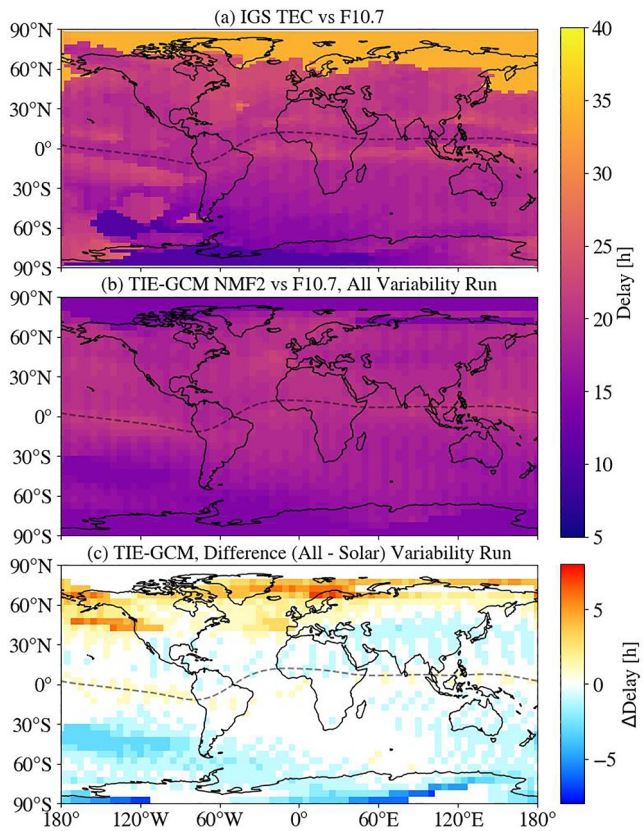

Figure 6. The spatial distribution of ionospheric delay is estimated using the F10.7 index alongside the IGS TEC and modeled NmF2. The upper panel illustrates the delay between the IGS TEC and the F10.7 index (a). The second panel depicts the delay using modeled NmF2 and the F10.7 index for the All Variability Run (b). The lower panel shows the modeled differences between the All Variability Run and the Solar Variability Run (c).

The ionospheric delay strongly depends on the solar activity conditions that leads to change in ion production and loss processes (Schmölter & von Savigny, 2022). These processes vary with altitude and availability of neutrals. The altitude dependence of the ionospheric delayed response has previously been discussed by Vaishnav et al. (2022); Schmölter et al. (2022). However, it is also important to understand the change in altitude response of the ionospheric delay due to the geomagnetic activity changes. Figure 7a shows the distribution of the ionospheric delay between modeled Ne and F10.7 at 0°E as a function of latitude and altitude during the study period. The upper panel shows the ionospheric delay distribution of All Variability Run. The maximum delay in the case of All Variability Run is about 24 hr in the low-latitude region up to 400 km. A longer delay in the NH compared to the SH is observed. The difference between the NH and SH is mainly evident in the high-latitude regions where the delay is less than 15 hr above 300 km. The ionospheric delay increases with altitude in the low-latitude region and the results are consistent with the previous research (e.g., Schmölter et al., 2022; Vaishnav, Jacobi, et al., 2021), while it decreases in high-latitude region. The lower panel shows the difference plot between All Variability Run and Solar Variability Run (Figure 7b). Geomagnetic activity typically increases the ionospheric delay by 1–5 hr above 300 km in low- and mid-latitudes. The maximum difference is observed in the NH and SH mid- and high-latitude regions, where the delay difference is up to about 2–8 hr. Between 200 and 250 km in high latitudes, the increase of the delay decreases to 1–3 hr. Above 250 km, the delay in SH mid- and high-latitudes increases by 1–6 hr, while it decreases by 1–8 hr in NH.

Figure 7 shows the clear impact of the geomagnetic activity. However for this analysis, we focus only on the results at 0°E. Therefore, the impact of geomagnetic activity on the spatial and latitudinal distribution of the delay,

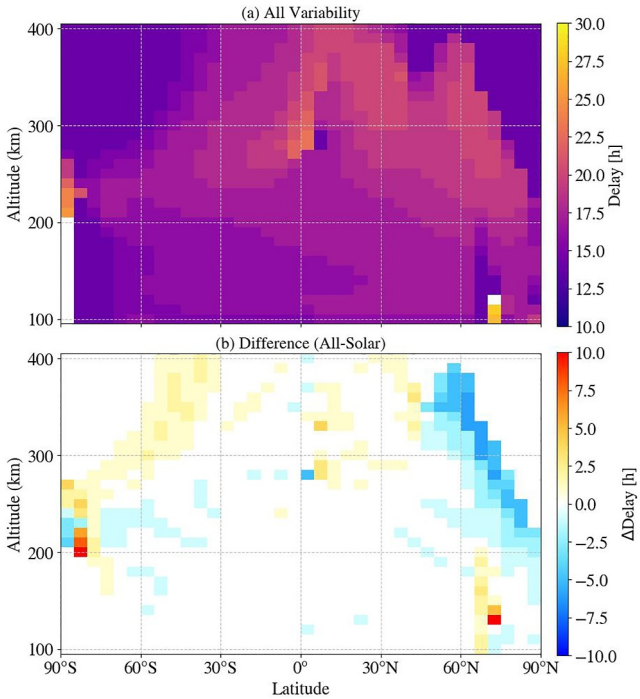

Figure 7. The latitude and altitude distribution of the ionospheric delay at 0°E is shown for TIE-GCM Ne with F10.7 in the All Variability Run (a), as well as the differences between the All Variability Run and the Solar Variability Run (b).

we further analyze the delay for the All variability Run and the Solar Variability Run at different altitudes (200, 250, 300, and 350 km) at different latitudes as shown in Figure 8. The spatial distribution of the ionospheric delay for All Variability Run along with the difference plot at 200 km, is shown in Figures 8a, and 8b. The difference plot does not show much variation except in high-latitude regions, where the delay slightly increases or decreases by about 1–4 hr. At 250 km altitude, a more positive delay of about 2–4 hr is observed compared to 200 km, while the NH high-latitude region exhibits a strong negative delay of about 2–6 hr (Figure 8d). Furthermore, the increased altitude leads to changes in the spatial distribution of the ionospheric delay (Figure 8f). In the SH high-latitude region, there is a more positive delay of about 2–5 hr, whereas it decreases slightly in the NH high-latitude region. At 350 km the ionospheric delay due to geomagnetic activity increase significantly on a global scale, including more delay in the SH as compared to the NH and to lower altitudes (Figure 8h). The maximum delay rises to about 5–8 hr. The analysis shows the ionospheric delay increases with altitude in low- and mid-latitude regions up to about 300 km, while the influence of geomagnetic activity introduces both spatial and altitude-dependent variations in the ionospheric delay.

Recently, Vaishnav, Jacobi, Schmölter, and Dühnen (2024) studied the impact of the lower atmospheric forcing on the delayed ionospheric response and its altitude dependence. They found a significant impact of the lower atmospheric forcing on the delayed ionospheric responses. The study reported smaller changes in delay below 250 km while maximum changes occurred above 250 km.

At the electron density peak, photoionization dominates due to strong EUV absorption, while photodissociation plays a more significant role at lower altitudes. This creates additional oxygen in the lower ionosphere, which then moves upward and increases O and O^+ at the F-region peak, thereby delaying the electron density response to changes in solar EUV flux (Dühnen et al., 2024; Jakowski et al., 1991; Schmölter et al., 2022; Schmölter & von Savigny, 2022).

The observed ionospheric delay is associated with changes in the TI compositions, as noted by several authors (Ren et al., 2018; Schmölter et al., 2020b; Vaishnav, Jacobi, et al., 2021). Therefore, it is important to investigate the vertical evolution of neutrals in the TI region during the study period and their contribution to the ionospheric delay.

We select day 15 of the study period, when geomagnetic activity is moderate (minimum Dst ≈ −66 nT). The peak solar activity occurs on day 14. To explore these differences, we calculate the percentage difference between day 15 and day 14 for the All Variability Run. Additionally, to examine the difference between the All Variability Run and the Solar Variability Run on day 15, we calculate the percentage difference between these two runs.

Figure 9 illustrates the latitude-height distributions of the O/N_2 ratio, the mass mixing ratios (mmr) of O and N_2, neutral temperature, and total mass density. The first column presents these parameters for day 15 of the All Variability Run at 0°E longitude. The geomagnetic activity-induced changes are calculated as a percentage difference ((All—Solar)/Solar). The second column shows the percentage difference between day 15 and day 14.

The O/N_2 ratio is a crucial parameter for studying changes induced by geomagnetic storms, as suggested by several authors (D. Strickland et al., 2004; Fuller-Rowell et al., 1994). The lower thermospheric concentrations of O and N_2 significantly affect the integrated O/N_2 ratio (D. J. Strickland et al., 1995; D. Strickland et al., 2004), leading to a strong correlation with the electron density in the F2 region of the middle thermosphere. Recently, Yu et al. (2023) explored the vertical evolution of neutral particles in the TI system during a geomagnetic storm. They found that regions with a decrease in the O/N_2 ratio are characterized by a decrease in the O mmr and an enhancement in the N_2 mmr. Conversely, regions with an increase in the O/N_2 ratio exhibit an increase in the O mmr and a decrease in the N_2 mmr. The current investigation yields somewhat similar results. The percentage difference in the O/N_2 ratio slightly increases in the mid-latitude region and decreases in the high-latitude region

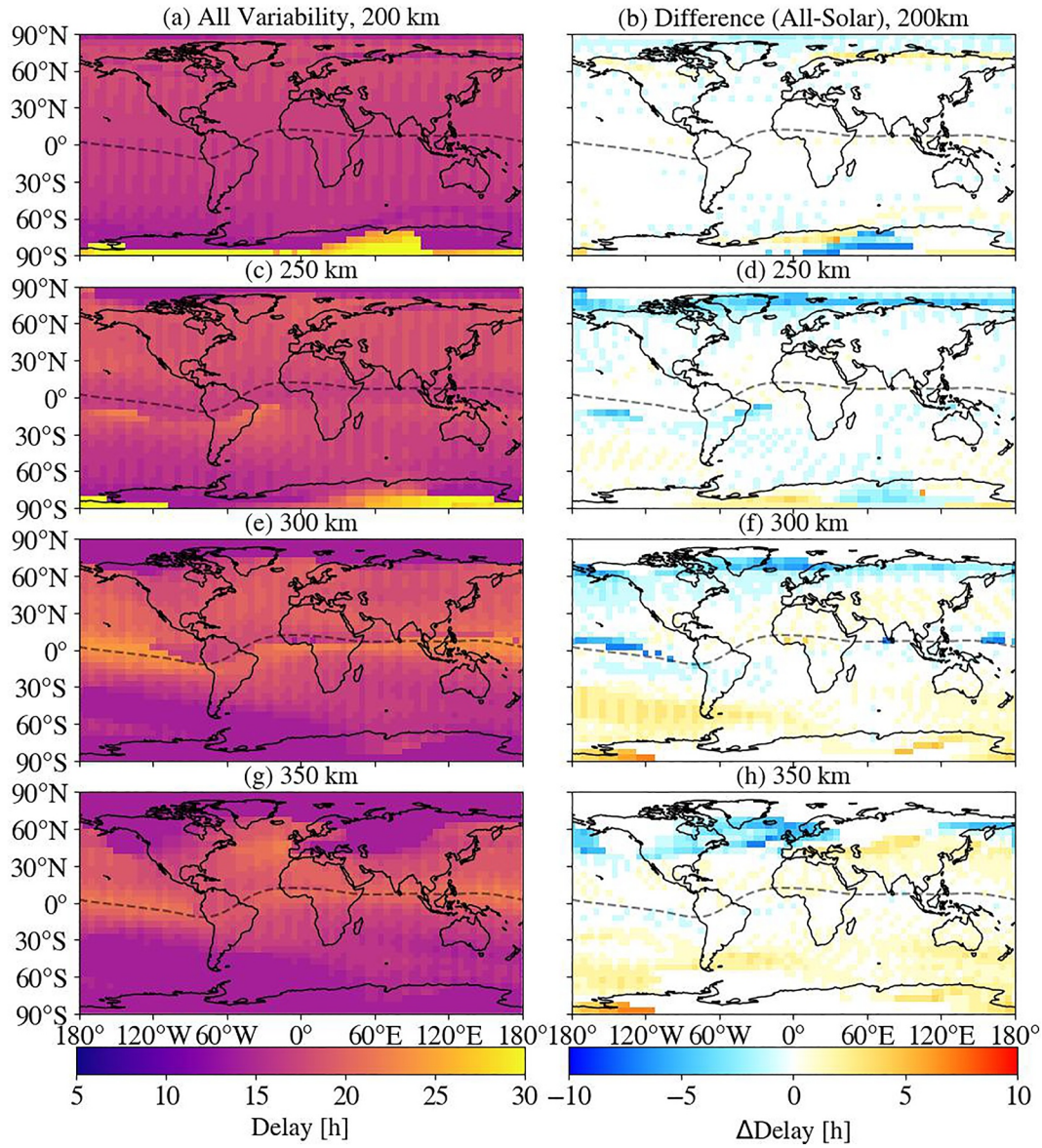

Figure 8. The spatial distribution of ionospheric delay is evaluated in relation to the F10.7 index and the modeled electron density (Ne) during the study period at various altitudes: 200, 250, 300, and 350 km. The first column (panels a, c, e, and f) presents the modeled delays from the All Variability Run. The third column (panels b, d, f, and h) shows the differences between the All Variability Run and the Solar Variability Run.

(Figure 9b). These changes align with the percentage variations in O (Figure 9e). Although solar activity peaks on day 14, moderate geomagnetic activity on day 15 leads to a slight increase in the O/N_2 ratio in low-latitude regions and a decrease in high-latitude regions.

On day 15, the percentage difference between the All and Solar Variability Runs exhibits similar behavior; however, the magnitude of the differences increases, despite solar activity remaining constant. This indicates a clear impact of geomagnetic activity, where the O/N_2 ratio again aligns with changes in O concentration. In contrast, the percentage change in N_2 shows opposite trends, as seen in the third row (Figure 9j), where N_2 increases by up to 250% in the high-latitude region above 300 km.

The analysis of O mmr and N_2 mmr indicates that increased temperatures lead to weak upwelling in high-latitude regions. This upwelling transports air from the lower to the upper thermosphere, resulting in an increase in N_2 mmr and a decrease in O mmr. Specifically, O mmr decreases by approximately 0%–60%, while N_2 mmr

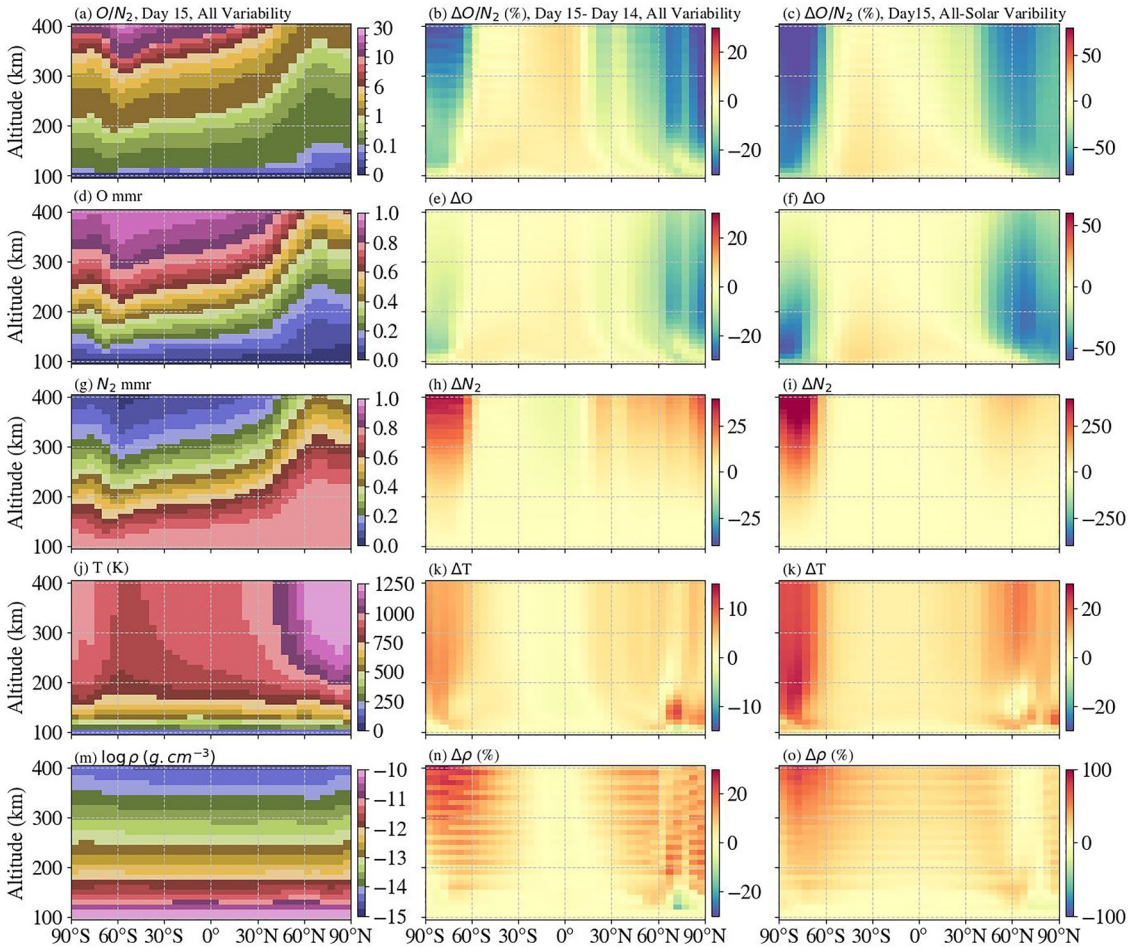

Figure 9. The evolution of TI parameters, including O/N_2, O, N_2 number density, temperature (T), and total mass density (ρ), is examined at 0° longitude as a function of latitude and altitude. The first column displays the results from the All Variability Run on day 15, while the second column indicates the percentage difference between day 15 and day 14 for the All Variability Run. The third column represents the percentage difference plot between the All Variability Run and the Solar Variability Run for day 15.

increases by about 250%. A slight increase in O mmr relative to N_2 mmr is also observed in the low-latitude region. The transport of N_2 and O reflects the influence of horizontal circulation effects (Burns et al., 2006). Geomagnetic activity disrupts the O/N_2 ratio due to enhanced neutral wind forcing (see Figure 2). During storm events, eastward zonal wind surges increase the O/N_2 ratio, while meridional winds exhibit strong equatorward flows that temporarily raise the O/N_2 levels before composition depletion takes over. Most importantly, storm-induced upwelling decreases the O/N_2 ratio between altitudes of 200–400 km.

By comparing the evolution of TI parameters specifically O, N_2, and the O/N_2 ratio along with the percentage changes between day 15 and day 14 (as shown in the middle column of Figure 6), we gain a better understanding of the conditions affecting ionospheric delay.

Between altitudes of 200–300 km in high-latitude regions, the ionospheric delay decreases to approximately 1–5 hr, which corresponds to a reduction in the O/N_2 ratio to about 10%–15%. In contrast, in low- and mid-latitude regions, the delay increases to around 1–3 hr, accompanied by an increase in the O/N_2 ratio to about 2%–7%. These results demonstrate that changes in ionospheric delay are strongly dependent on compositional variations driven by geomagnetic activity.

The TI changes are influenced by external factors such as solar activity, geomagnetic activity, and lower atmospheric forcing. During periods of low solar activity, lower atmospheric forcing plays a more significant role.

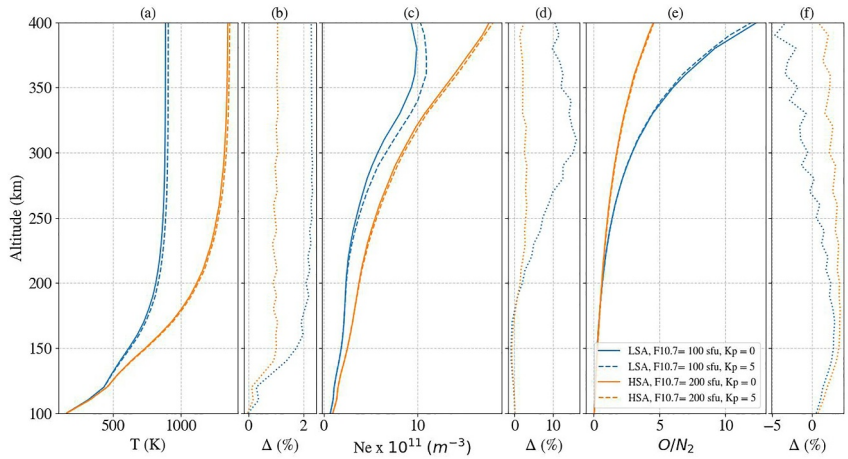

Figure 10. Panels (a), (c), and (e) show TIE-GCM simulations of neutral temperature, electron density, and the O/N_2 ratio at 0° latitude/longitude (12 UT) under low (blue, F10.7 = 100 sfu) and high (orange, F10.7 = 200 sfu) solar activity for Kp = 5 (dashed) and Kp = 0 (solid) runs. Panels (b), (d), and (f) show the corresponding percentage differences between the two runs for low (blue dotted) and high (orange dotted) solar activity. F10.7 and Kp values are indicated in the figure.

In contrast, during moderate and high solar activity, geomagnetic activity significantly contributes to the neutral composition of the atmosphere.

To explore this further, we conducted numerical simulations under four different conditions: low solar activity (F10.7 = 100 sfu) and high solar activity (F10.7 = 200 sfu), as well as quiet geomagnetic conditions (Kp = 0) and moderate geomagnetic conditions (Kp = 5).

Figure 10 illustrates the variability in neutral temperature, electron density, and O/N_2 ratio along with the difference plot between Kp = 5 and Kp = 0 Runs during the specified conditions at 0° latitude and longitude at 12 UT.

The neutral temperature increases with altitude, highlighting distinct differences between low and high solar activity for both Kp = 5 and Kp = 0 (Figure 10a). Neutral temperature increases by about 40% above 200 km when comparing low and high solar activity under Kp = 0. Under low solar activity, the temperature rises slightly by about 2% above 200 km when comparing Kp = 5 to Kp = 0, while under high solar activity, the increase is about 1% (Figure 10b).

Figure 10c shows electron density profiles for both solar activity conditions. Similar to temperature, electron density increases by about 8%–10% above 250 km during the Kp = 5 Run under low solar activity (Figure 10d). However, under high solar activity, geomagnetic effects are less pronounced due to the dominant influence of solar activity.

Furthermore, we investigate the behavior of the O/N_2 ratio during both low and high solar activity conditions (Figure 10e). Due to changes in solar and geomagnetic activity, the O/N_2 ratio changes, reflecting variations in neutral composition. We calculate the O/N_2 ratio using the densities of O and N_2 at a fixed height. The O/N_2 ratio increases with altitude but decreases with solar activity. This decrease occurs because increased solar activity expands the thermosphere, causing upwelling that lifts heavier N_2 to higher altitudes, resulting in a lower O/N_2 ratio.

During low solar activity conditions for the Kp = 5 Run, the O/N_2 ratio slightly decreases above 250 km, while during high solar activity, it slightly increases (Figure 10f).

4. Discussion and Conclusions

We use the Thermosphere-Ionosphere-Electrodynamics General Circulation Model (TIE-GCM) to investigate the impact of geomagnetic activity on the vertical variations of the delayed ionospheric response. Our analysis focuses on the O/N_2 ratio and neutral densities at different altitude levels during a period of moderate solar and geomagnetic activity, specifically from 29 April to 25 May 2015.

We conduct the model analysis under two distinct conditions. The first condition, labeled "All Variability," includes all sources of variability, encompassing both solar and geomagnetic activity. The second condition, termed "Solar Variability," excludes geomagnetic activity by setting Kp to zero. This approach enables us to gain insights into the specific impacts of geomagnetic activity.

The IGS TEC shows an ionospheric delay of about 18 hr with respect to F10.7 variations, with higher delays (30–40 hr) in NH high-latitudes and lower (5–15 hr) delay in SH high-latitudes. The analysis of peak electron density (NmF2) simulated using TIE-GCM shows similar patterns with an average delay of about 17 hr for the All Variability Run. The calculated delay for both the model and observed ionospheric parameters is in good agreement with the preceding studies (e.g., Dühnen et al., 2024; Schmölter et al., 2018, 2020b; Vaishnav et al., 2022; Vaishnav, Jacobi, Schmölter, & Dühnen, 2024; Vaishnav, Jacobi, et al., 2021). Comparing All and Solar Variability runs, geomagnetic activity increases the delay by 3–7 hr in NH high-latitudes and decreases it by 1–5 hr elsewhere, showing its varying latitudinal impact (see Figure 6).

The All Variability Run shows a maximum ionospheric delay of about 24 hr in low-latitude regions up to 300 km, with the NH experiences greater delays than the SH. In high-latitude areas above 300 km, delays remain under 15 hr. Analysis of the Solar Variability Run indicates that geomagnetic activity increases ionospheric delays by 1–5 hr in low- and mid-latitude regions above 300 km, peaking at 2–5 hr in the SH. In high-latitude regions, delays drop to 1–5 hr (see Figures 7 and 8). The study shows ionospheric delay varies with moderate geomagnetic activity and is the first to confirm its effect on vertical variations of the delayed ionospheric response. Previously, Vaishnav, Jacobi, Schmölter, and Dühnen (2024) examined vertical variations driven by lower atmospheric forcing.

The comparison between these runs shows that the geomagnetic activity alters the ionospheric composition both vertically and horizontally. The simulations show that the ionospheric delay decreases when the geomagnetic activity conditions are included in the model. In addition, we focus on the variations in the O/N_2 ratio, which increases with rising solar flux. The model simulation with geomagnetic activity shows a lower O/N_2 than the results with low geomagnetic conditions. This suggests that O/N_2 increases with solar irradiance when geomagnetic activity is low, thereby increasing ionospheric delay.

This study aims to evaluate a model's ability to simulate moderate geomagnetic activity through controlled runs. It confirms previous findings and highlights the significant role of geomagnetic activity in delayed ionospheric response (e.g., Ren et al., 2018; Schmölter et al., 2020a, 2020b; Vaishnav et al., 2022). Future work will extend to geomagnetic storm activity and explicitly include the effect of varying lower atmospheric forcing.

The results may be summarized as follows.

- The thermosphere-ionosphere composition varies both vertically and horizontally in response to changes in geomagnetic activity.
- The TIE-GCM All Variability Run shows an ionospheric delay of approximately 17 hr. Geomagnetic activity increases this delay by 2–6 hr in NH high-latitude region and decreases it to 1–5 hr at other latitudes.
- Ionospheric delay increases with altitude, particularly 3–8 hr above 300 km, and is strongly influenced by geomagnetic activity.
- Changes in ionospheric delay closely follow variations in the O/N_2 ratio.

Conflict of Interest

The authors declare no conflicts of interest relevant to this study.

Data Availability Statement

IGS TEC maps can be downloaded from https://cddis.nasa.gov/archive/gnss/products/ionex/ (NASA, 2025a). Geomagnetic indices have been downloaded from https://omniweb.gsfc.nasa.gov/form/dx1.html (NASA, 2025b). The F10.7 index at 1 AU have been obtained from the LISIRD database (LASP, 2025, https://lasp.colorado.edu/lisird/). The TIE-GCM simulation data used for this work can be accessed at https://doi.org/10.5281/zenodo.15487630 (Vaishnav, 2025).

Acknowledgments
The study has been supported by Deutsche Forschungsgemeinschaft (DFG, German Research Foundation) under project no. 495912049. Open Access funding enabled and organized by Projekt DEAL.

References

Afraimovich, E. L., Astafyeva, E. I., Oinats, A. V., Yasukevich, Y. V., & Zhivetiev, I. V. (2008). Global electron content: A new conception to track solar activity. *Annales Geophysicae*, *26*(2), 335–344. https://doi.org/10.5194/angeo-26-335-2008

Anderson, P. C., & Hawkins, J. M. (2016). Topside ionospheric response to solar EUV variability. *Journal of Geophysical Research: Space Physics*, *121*(2), 1518–1529. https://doi.org/10.1002/2015ja021202

Burns, A., Killeen, T., Wang, W., & Roble, R. (2004). The solar-cycle-dependent response of the thermosphere to geomagnetic storms. *Journal of Atmospheric and Solar-Terrestrial Physics*, *66*(1), 1–14. https://doi.org/10.1016/j.jastp.2003.09.015

Burns, A., Wang, W., Killeen, T., Solomon, S., & Wiltberger, M. (2006). Vertical variations in the N_2 mass mixing ratio during a thermospheric storm that have been simulated using a coupled magnetosphere-ionosphere-thermosphere model. *Journal of Geophysical Research*, *111*(A11), A11309. https://doi.org/10.1029/2006JA011746

Cai, X., Burns, A. G., Wang, W., Qian, L., Solomon, S. C., Eastes, R. W., et al. (2021). Investigation of a neutral "Tongue" observed by GOLD during the geomagnetic storm on May 11, 2019. *Journal of Geophysical Research: Space Physics*, *126*(6), e2020JA028817. https://doi.org/10.1029/2020ja028817

Chen, Y., Liu, L., & Wan, W. (2012). The discrepancy in solar EUV-proxy correlations on solar cycle and solar rotation timescales and its manifestation in the ionosphere. *Journal of Geophysical Research*, *117*(A3), A03313. https://doi.org/10.1029/2011ja017224

Dühnen, H., Vaishnav, R., Jacobi, C., Schmölter, E., & Berdermann, J. (2024). Comparative case study of delayed ionospheric response to a superposed 27-day solar rotation signal. *Advances in Space Research*, 3115–3132. https://doi.org/10.1016/j.asr.2024.12.004

Fang, T.-W., Akmaev, R., Fuller-Rowell, T., Wu, F., Maruyama, N., & Millward, G. (2013). Longitudinal and day-to-day variability in the ionosphere from lower atmosphere tidal forcing. *Geophysical Research Letters*, *40*(11), 2523–2528. https://doi.org/10.1002/grl.50550

Field, P., Rishbeth, H., Moffett, R., Wenden, D., Fuller-Rowell, T., Millward, G., & Aylward, A. (1998). Modelling composition changes in f-layer storms. *Journal of Atmospheric and Solar-Terrestrial Physics*, *60*(5), 523–543. https://doi.org/10.1016/S1364-6826(97)00074-6

Forbes, J. M., Palo, S. E., & Zhang, X. (2000). Variability of the ionosphere. *Journal of Atmospheric and Solar-Terrestrial Physics*, *62*(8), 685–693. https://doi.org/10.1016/s1364-6826(00)00029-8

Fuller-Rowell, T., Codrescu, M., Moffett, R., & Quegan, S. (1994). Response of the thermosphere and ionosphere to geomagnetic storms. *Journal of Geophysical Research*, *99*(A3), 3893–3914. https://doi.org/10.1029/93JA02015

Heelis, R., Lowell, J. K., & Spiro, R. W. (1982). A model of the high-latitude ionospheric convection pattern. *Journal of Geophysical Research*, *87*(A8), 6339–6345. https://doi.org/10.1029/JA087iA08p06339

Hernández-Pajares, M., Juan, J. M., Sanz, J., Orus, R., Garcia-Rigo, A., Feltens, J., et al. (2009). The IGS VTEC maps: A reliable source of ionospheric information since 1998. *Journal of Geodesy*, *83*(3–4), 263–275. https://doi.org/10.1007/s00190-008-0266-1

Jacobi, C., Jakowski, N., Schmidtke, G., & Woods, T. N. (2016). Delayed response of the global total electron content to solar EUV variations. *Advances in Radio Science*, *14*, 175–180. https://doi.org/10.5194/ars-14-175-2016

Jakowski, N., Fichtelmann, B., & Jungstand, A. (1991). Solar activity control of ionospheric and thermospheric processes. *Journal of Atmospheric and Terrestrial Physics*, *53*(11–12), 1125–1130. https://doi.org/10.1016/0021-9169(91)90061-b

Kutiev, I., Tsagouri, I., Perrone, L., Pancheva, D., Mukhtarov, P., Mikhailov, A., et al. (2013). Solar activity impact on the Earth's upper atmosphere. *Journal of Space Weather and Space Climate*, *3*, A06. https://doi.org/10.1051/swsc/2013028

LASP. (2025). LASP interactive solar irradiance data center [Dataset]. *University of Colorado*. Retrieved from https://lasp.colorado.edu/lisird/

Li, J., Wang, W., Lu, J., Yue, J., Burns, A. G., Yuan, T., et al. (2019). A modeling study of the responses of mesosphere and lower thermosphere winds to geomagnetic storms at middle latitudes. *Journal of Geophysical Research: Space Physics*, *124*(5), 3666–3680. https://doi.org/10.1029/2019JA026533

Liu, L., Wan, W., Ning, B., Pirog, O. M., & Kurkin, V. I. (2006). Solar activity variations of the ionospheric peak electron density. *Journal of Geophysical Research*, *111*(A8), A08304. https://doi.org/10.1029/2006ja011598

NASA. (2025a). GNSS atmospheric products [Dataset]. Retrieved from http://cddis.nasa.gov/Data_and_Derived_Products/GNSS/atmospheric_products.html

NASA. (2025b). Omniweb plus database [Dataset]. Retrieved from http://omniweb.gsfc.nasa.gov/

Qian, L., Burns, A. G., Emery, B. A., Foster, B., Lu, G., Maute, A., et al. (2014). The NCAR TIE-GCM: A community model of the coupled thermosphere/ionosphere system. Modeling the ionosphere–thermosphere system (pp. 73–83). https://doi.org/10.1002/9781118704417.ch7

Qian, L., Gan, Q., Wang, W., Cai, X., Eastes, R., & Yue, J. (2022). Seasonal variation of thermospheric composition observed by NASA GOLD. *Journal of Geophysical Research*, *127*(6), e2022JA030496. https://doi.org/10.1029/2022ja030496

Qian, L., Wang, W., Burns, A. G., Chamberlin, P. C., & Solomon, S. C. (2020). Responses of the thermosphere and ionosphere system to concurrent solar flares and geomagnetic storms. *Journal of Geophysical Research: Space Physics*, *125*(3), e2019JA027431. https://doi.org/10.1029/2019JA027431

Ren, D., Lei, J., Wang, W., Burns, A., Luan, X., & Dou, X. (2018). Does the peak response of the ionospheric F2 region plasma lag the peak of 27-day solar flux variation by multiple days? *Journal of Geophysical Research: Space Physics*, *123*(9), 7906–7916. https://doi.org/10.1029/2018ja025835

Ren, D., Lei, J., Wang, W., Burns, A., Luan, X., & Dou, X. (2019). A simulation study on the time delay of daytime thermospheric temperature response to the 27-day solar EUV flux variation. *Journal of Geophysical Research: Space Physics*, *124*(11), 9184–9193. https://doi.org/10.1029/2019ja027000

Richards, P. G., Fennelly, J. A., & Torr, D. G. (1994). EUVAC: A solar EUV flux model for aeronomic calculations. *Journal of Geophysical Research*, *99*(A5), 8981–8992. https://doi.org/10.1029/94ja00518

Richmond, A. D., & Maute, A. (2014). Ionospheric electrodynamics modeling. Modeling the ionosphere–thermosphere system (pp. 57–71). https://doi.org/10.1002/9781118704417.ch6

Richmond, A. D., Ridley, E. C., & Roble, R. G. (1992). A thermosphere/ionosphere general circulation model with coupled electrodynamics. *Geophysical Research Letters*, *19*(6), 601–604. https://doi.org/10.1029/92gl00401

Rishbeth, H. (1998). How the thermospheric circulation affects the ionospheric F2 layer. *Journal of Atmospheric and Solar-Terrestrial Physics*, *60*(14), 1385–1402. https://doi.org/10.1016/s1364-6826(98)00062-5

Rishbeth, H., & Mendillo, M. (2001). Patterns of F2-layer variability. *Journal of Atmospheric and Solar-Terrestrial Physics*, *63*(15), 1661–1680. https://doi.org/10.1016/s1364-6826(01)00036-0

Rishbeth, H., Sedgemore-Schulthess, K. J. F., & Ulich, T. (2000). Semiannual and annual variations in the height of the ionospheric F2-peak. *Annales Geophysicae*, *18*(3), 285–299. https://doi.org/10.1007/s00585-000-0285-6

Roble, R., & Ridley, E. (1987). An auroral model for the NCAR thermospheric general circulation model (TGCM). In *Annales geophysicae* (Vol. 5, pp. 369–382).

Schmölter, E., Berdermann, J., & Codrescu, M. (2021). The delayed ionospheric response to the 27-day solar rotation period analyzed with GOLD and IGS TEC data. *Journal of Geophysical Research: Space Physics*, *126*(2), e2020JA028861. https://doi.org/10.1029/2020ja028861

Schmölter, E., Berdermann, J., Jakowski, N., & Jacobi, C. (2020a). Modeling of the delayed ionospheric response with the TIE-GCM model. In *2020 european navigation conference (ENC)* (pp. 1–9). https://doi.org/10.23919/ENC48637.2020.9317355

Schmölter, E., Berdermann, J., Jakowski, N., & Jacobi, C. (2020b). Spatial and seasonal effects on the delayed ionospheric response to solar EUV changes. *Annales Geophysicae*, *38*(1), 149–162. https://doi.org/10.5194/angeo-38-149-2020

Schmölter, E., Berdermann, J., Jakowski, N., Jacobi, C., & Vaishnav, R. (2018). Delayed response of the ionosphere to solar EUV variability. *Advances in Radio Science*, *16*, 149–155. https://doi.org/10.5194/ars-16-149-2018

Schmölter, E., Dühnen, H., Berdermann, J., Vaishnav, R., & Jacobi, C. (2024). Spatial features of the delayed ionospheric response during low and high solar activity. *Journal of Geophysical Research: Space Physics*, *129*(5), e2024JA032672. https://doi.org/10.1029/2024JA032672

Schmölter, E., Heymann, F., Savigny, C., & Berdermann, J. (2022). The height-dependent delayed ionospheric response to solar EUV. *Journal of Geophysical Research: Space Physics*, *127*(3), e2021JA030118. https://doi.org/10.1029/2021ja030118

Schmölter, E., & von Savigny, C. (2022). Solar activity driven 27-day signatures in ionospheric electron and molecular oxygen densities. *Journal of Geophysical Research: Space Physics*, *127*(9), e2022JA030671. https://doi.org/10.1029/2022ja030671

Strickland, D., Meier, R., Walterscheid, R., Craven, J., Christensen, A., Paxton, L., et al. (2004). Quiet-time seasonal behavior of the thermosphere seen in the far ultraviolet dayglow. *Journal of Geophysical Research*, *109*(A1), A01302. https://doi.org/10.1029/2003JA010220

Strickland, D. J., Evans, J. S., & Paxton, L. J. (1995). Satellite remote sensing of thermospheric O/N_2 and solar EUV: 1. theory. *Journal of Geophysical Research*, *100*(A7), 12217–12226. https://doi.org/10.1029/95ja00574

Sutton, E., Forbes, J., & Knipp, D. (2009). Rapid response of the thermosphere to variations in joule heating. *Journal of Geophysical Research*, *114*(A4). https://doi.org/10.1016/j.jastp.2004.03.026

Thayer, J. P., & Semeter, J. (2004). The convergence of magnetospheric energy flux in the polar atmosphere. *Journal of Atmospheric and Solar-Terrestrial Physics*, *66*(10), 807–824. https://doi.org/10.1016/j.jastp.2004.01.035

Vaishnav, R. (2025). TIE-GCM simulations [Dataset]. *Zenodo*. https://doi.org/10.5281/zenodo.15487630

Vaishnav, R., Jacobi, C., & Berdermann, J. (2019). Long-term trends in the ionospheric response to solar extreme-ultraviolet variations. *Annales Geophysicae*, *37*(6), 1141–1159. https://doi.org/10.5194/angeo-37-1141-2019

Vaishnav, R., Jacobi, C., Berdermann, J., Codrescu, M., & Schmölter, E. (2021). Role of eddy diffusion in the delayed ionospheric response to solar flux changes. *Annales Geophysicae*, *39*(4), 641–655. https://doi.org/10.5194/angeo-39-641-2021

Vaishnav, R., Jacobi, C., Berdermann, J., Schmölter, E., & Codrescu, M. (2018). Ionospheric response to solar EUV variations: Preliminary results. *Advances in Radio Science*, *16*, 157–165. https://doi.org/10.5194/ars-16-157-2018

Vaishnav, R., Jacobi, C., Berdermann, J., Schmölter, E., & Codrescu, M. (2022). Delayed ionospheric response to solar extreme ultraviolet radiation variations: A modeling approach. *Advances in Space Research*, *69*(6), 2460–2476. https://doi.org/10.1016/j.asr.2021.12.041

Vaishnav, R., Jacobi, C., Berdermann, J., Schmölter, E., Dühnen, H., & Codrescu, M. (2024). Ionospheric response to solar EUV radiation variations using GOLD observations and the CTIPe model. *Journal of Geophysical Research: Space Physics*, *129*(1), e2022JA030887. https://doi.org/10.1029/2022JA030887

Vaishnav, R., Jacobi, C., Schmölter, E., & Dühnen, H. (2024a). Influence of lower atmospheric variability: An investigation of delayed ionospheric response to solar activity. *Journal of Geophysical Research: Space Physics*, *129*(11), e2024JA032999. https://doi.org/10.1029/2024JA032999

Vaishnav, R., Schmölter, E., Jacobi, C., Berdermann, J., & Codrescu, M. (2021). Ionospheric response to solar extreme ultraviolet radiation variations: Comparison based on CTIPe model simulations and satellite measurements. *Annales Geophysicae*, *39*(2), 341–355. https://doi.org/10.5194/angeo-39-341-2021

Wang, W., Burns, A., Wiltberger, M., Solomon, S., & Killeen, T. (2008). Altitude variations of the horizontal thermospheric winds during geomagnetic storms. *Journal of Geophysical Research*, *113*(A2), A02301. https://doi.org/10.1029/2007JA012374

Yamazaki, Y., & Richmond, A. D. (2013). A theory of ionospheric response to upward-propagating tides: Electrodynamic effects and tidal mixing effects. *Journal of Geophysical Research: Space Physics*, *118*(9), 5891–5905. https://doi.org/10.1002/jgra.50487

Yu, T., Wang, W., Ren, Z., Cai, X., & He, M. (2023). Vertical variations in thermospheric O/N_2 and the relationship between O and N_2 perturbations during a geomagnetic storm. *Earth and Space Science*, *10*(10), e2023EA002988. https://doi.org/10.1029/2023EA002988